High-Cloud Horizontal Inhomogeneity and Solar Albedo Bias

BETTY CARLIN

Department of Physics and Atmospheric Science, Dalhousie University, Halifax, Nova Scotia, Canada

QIANG FU

Department of Oceanography, Dalhousie University, Halifax, Nova Scotia, Canada, and Department of Atmospheric Sciences, University of Washington, Seattle, Washington

ULRIKE LOHMANN

Department of Physics and Atmospheric Science, Dalhousie University, Halifax, Nova Scotia, Canada

GERALD G. MACE AND KENNETH SASSEN

Department of Atmospheric Sciences, University of Utah, Salt Lake City, Utah

JENNIFER M. COMSTOCK

Pacific Northwest National Laboratory, Richland, Washington

(Manuscript received 24 April 2001, in final form 15 January 2002)

ABSTRACT

High ice cloud horizontal inhomogeneity is examined using optical depth retrievals from four midlatitude datasets. Three datasets include ice cloud microphysical profiles derived from millimeter cloud radar at the Southern Great Plains Atmospheric Radiation Measurement site in Oklahoma. A fourth dataset combines lidar and midinfrared radiometry (LIRAD), and is from the Facility for Atmospheric Remote Sensing at the University of Utah, Salt Lake City, Utah. Plane-parallel homogeneous (PPH) calculations of domain-averaged solar albedo for these four datasets are compared to independent column approximation (ICA) results. A solar albedo bias up to 25% is found over a low reflective surface at a high solar zenith angle. A spherical solar albedo bias as high as 11% is shown. The gamma-weighted radiative transfer (GWRT) scheme is shown to be an effective correction for the solar albedo bias suitable for GCM applications. The GWRT result was, in all cases, within 1–2 W m^{-2} of the ICA outgoing solar flux. The GWRT requires a parameterization of the standard deviation of cloud optical depth. It is suggested that the domain-averaged cloud optical depth and ice water path together can be used in a parameterization to account for 80% of the standard deviation in optical depth.

1. Introduction

Clouds play an important role in the radiative energy budget of the earth–atmosphere system. The domain-averaged radiative flux calculation of a general circulation model (GCM) depends strongly on cloud representation. However, clouds exhibit dramatic variabilities at spatial scales smaller than the typical grid cell of these large-scale models used to study climate. When cloud subgrid-scale variability is neglected, significant errors can occur in radiative flux calculations (Harshvardhan and Randall 1985; Stephens 1985; Cahalan et al. 1994a; Barker 1996a; Pincus et al. 1999). Some decades ago, Weinman and Swarztrauber (1968) pointed out that ''a deeply stratified medium of a given mean optical thickness has a lower mean albedo than a horizontally homogeneous medium of the same mean optical thickness.'' Yet at present, most GCMs still consider clouds to be horizontally homogeneous over the fraction of the grid-box layer that they occupy. Thus, a GCM has to use an unrealistically small liquid water content to produce a realistic solar albedo as a consequence of the plane-parallel homogeneous cloud assumption (e.g., Harshvardan and Randall 1985).

Considerable research has gone into the investigation of solar radiative transfer for horizontally inhomogeneous clouds (Stephens 1988; Evans 1993; Cahalan et al. 1994a; Barker 1996b; Oreopoulos and Davies

Corresponding author address: Betty Carlin, Atmospheric Science Program, Department of Physics, Dalhousie University, Halifax, NS B3H 3J5, Canada.
E-mail: bcarlin@atm.dal.ca

1998a). Techniques are being developed to correct the plane-parallel homogeneous (PPH) bias. Rescaling of the cloud liquid water path and the use of probability density functions to represent cloud horizontal inhomogeneity have been suggested (Cahalan et al. 1994a; Barker 1996a). Parameterizations to represent cloud subgrid-scale variability are being investigated (Tiedke 1996; Considine et al. 1997; Pincus et al. 1999). Efficient solar radiative transfer schemes, which treat cloud horizontal inhomogeneity, are also being developed (Oreopoulos and Barker 1999; Barker and Fu 1999; Barker and Fu 2000; Cairns et al. 2000).

Work over the past few years has focussed on quantifying the solar albedo bias for stratocumulus cloud decks. A bias as high as 15% has been reported for these clouds (Cahalan et al. 1994a; Barker 1996b; Pincus et al. 1999). This study investigates high-cloud horizontal inhomogeneity and the associated radiative energy bias. By high clouds, we refer to clouds with tops above 440 hPa (Hartmann et al. 1992; Hahn et al. 2001). In the midlatitudes, such clouds have temperatures considerably colder than the earth surface, and thus, are ice clouds. We prefer to use the term high clouds to distinguish the ice clouds studied here from the ice clouds that may occur at lower altitudes in the midlatitude winter and polar regions. The high clouds examined include cirrus (Sassen and Cho 1992; Sassen 2001) and other optically thicker clouds, but all with an optical depth of 5 or less. Sassen and Cho (1992) limited cirrus optical depth to less than 3. High clouds of vertical extent (i.e., having very low bases) are not included in the datasets presented here.

High clouds play an important role in the radiative budget of the earth–atmosphere system in terms of reflection of solar radiation and trapping of outgoing longwave radiation (Ackerman et al. 1988; Stephens et al. 1990; Hartmann et al. 1992; Lohmann and Roeckner 1995). Attention has recently been given to longwave radiative transfer through horizontally inhomogeneous high ice cloud fields. A bias in the outgoing longwave radiative energy budget, up to -15 W m^{-2}, has been found (Fu et al. 2000a; Pomroy and Illingworth 2000). Here we focus on the companion problem for high clouds, the solar albedo bias.

In this study, we start with a discussion of the nonlinear relationship between solar albedo and high ice cloud optical depth (section 2). As a consequence of the nonlinearity, a solar albedo bias will result when cloud optical depth subgrid-scale variability is neglected. Four high ice cloud datasets are presented (section 3). One is derived from lidar and three are from millimeter cloud radar (MMCR). These datasets are used to estimate the subgrid-scale variability in high ice cloud optical depth. The independent column approximation (ICA; Cahalan et al. 1994b; Barker 1996a; Fu et al. 2000b) is then used to investigate the solar albedo bias due to the PPH assumption.

Using the four cloud datasets, we then demonstrate the efficacy of the gamma-weighted radiative transfer scheme (GWRT; Barker 1996a) as a means of accounting for the high-cloud subgrid-scale variability (section 4). The two parameters required by this scheme are the mean cloud optical depth and the standard deviation of optical depth. The ensuing problem in application to large-scale models is that while the mean cloud optical depth is readily available, the standard deviation of optical depth is not. One of the MMCR datasets is used to investigate the relationship between the standard deviation of optical depth and parameters readily available in a GCM including the following domain-averaged quantities: cloud-base and -top heights, midcloud height, cloud thickness, particle size, ice water content, ice water path, and optical depth (section 5). The last section is the summary and conclusions.

2. Solar albedo and high-cloud optical depth relationship

The nonlinear relationship between cloud optical depth and solar albedo is the crux of the solar albedo bias problem. Here, we investigate this relationship for high ice clouds. We define solar albedo as the ratio of the reflected to the incident broadband solar flux at the top of the atmosphere. The system considered contains clouds, atmospheric molecules, and an earth surface. The solar albedo is then a function of cloud optical depth, atmospheric optical depth, underlying surface albedo, and solar zenith angle.

In this study we use the radiation model developed by Fu and Liou (1992, 1993). The radiative transfer scheme used in this model is the delta-four-stream approximation. Nongray gaseous absorption due to H_2O, CO_2, O_3, CH_4, and N_2O is incorporated into the scattering atmosphere using the correlated *k*-distribution method. For ice clouds, the single-scattering properties for nonspherical ice crystals are parameterized based on geometric ray tracing and finite-difference time-domain techniques (Fu 1996; Fu et al. 1998). The *U.S. Standard Atmosphere, 1976* is used for vertical profiles of pressure, temperature, water vapor, and ozone.

Figure 1 shows the broadband solar albedo as a function of ice cloud optical depth for an ice cloud located in the 9–11-km layer. This is a one-dimensional calculation. For solar radiative transfer, unlike infrared transfer, the cloud-base and -top heights are of minor importance. In this study, we therefore assume all high ice clouds to be located in a layer between 9 and 11 km. Solar albedos are shown for different combinations of solar zenith angle and underlying constant surface albedo. The surface albedos of 0.05, 0.3, and 0.8 roughly correspond to ocean, desert, and new snow, respectively (Briegleb and Ramanathan 1982). We also consider the situation for high clouds above a thick low cloud between 1 and 4 km. Note that in all cases with a constant surface albedo, above a certain cloud optical depth, there is a convex relationship between solar albedo and ice

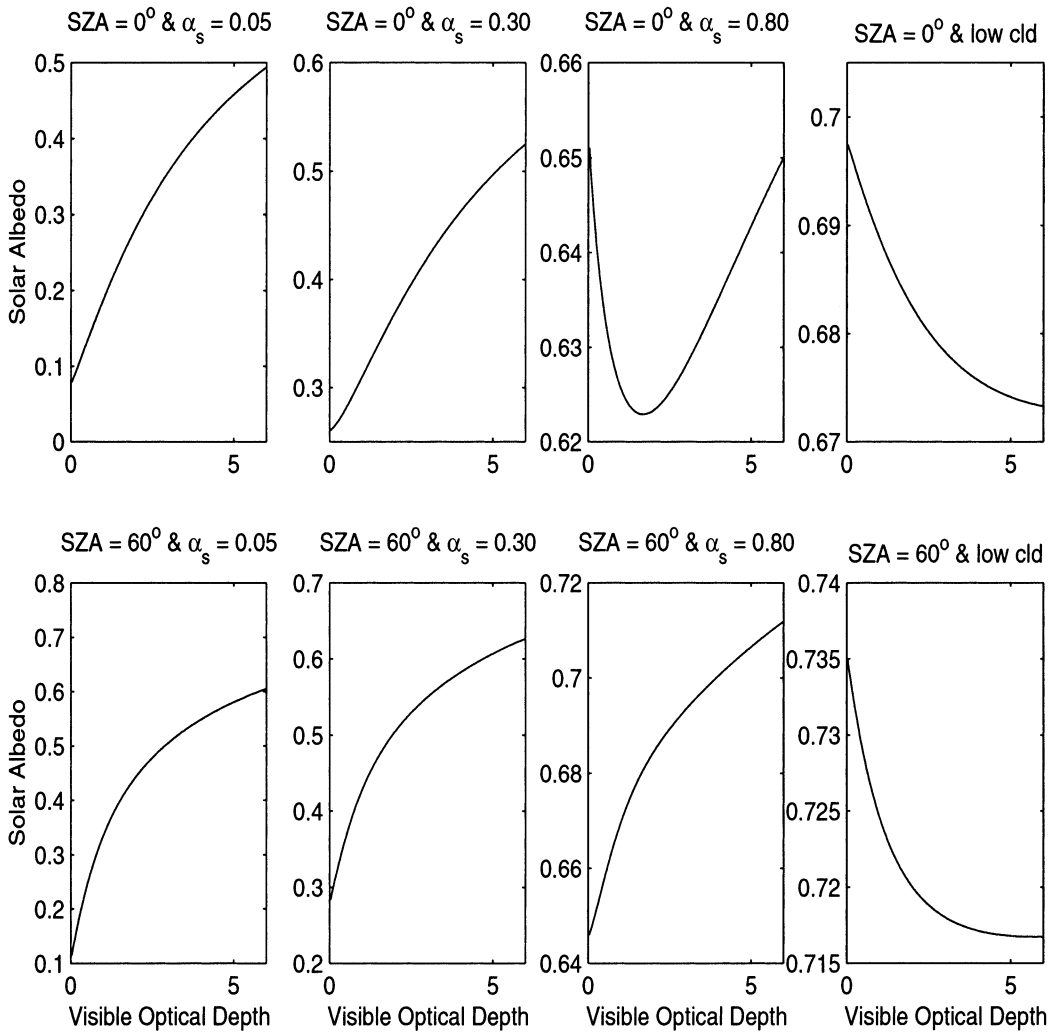

FIG. 1. Solar albedo as a function of high ice cloud optical depth. Shown are plots for SZAs of 0° and 60° combined with underlying surface albedo, α_s, of 0.05, 0.3, 0.8, and a thick low cloud (LWC = 0.2 g m^{-3}) in the 1–4-km layer.

cloud optical depth. However, under certain scenarios, there is a concave relationship at low optical depths. This is particularly noticeable for an overhead sun and a high reflective underlying surface. For high ice clouds above thick low clouds, concave curves are observed.

The convex curves are readily understood. Scattering increases with cloud optical depth to approach a limit determined by the amount of incident energy. To examine the concave curve case, we present Fig. 2, which shows the albedo in each solar band of the Fu–Liou radiation model for the overhead sun and high reflective underlying surface case. The solar bands are over ranges of 0.20–0.69, 0.69–1.30, 1.30–1.90, 1.90–2.50, 2.50–3.50, and 3.50–4.00 μm. The energy in each solar band respectively is 629.0, 491.7, 152.1, 49.4, 32.2, and 5.2 W m^{-2}. Scattering is conservative in the first band and is also a dominant process in the second band. The last two bands are nonscattering and the middle two include nonconservative scattering. The concave nature of the broadband curve is a combination of the effects of cloud scattering and absorption above highly reflective surfaces. As the cloud thickens optically, the cloud absorbs more photons above the reflective surface. This results in the decreasing solar albedo with increasing cloud optical depth seen in the last four bands. The conservative scattering process for a cloud in an optically transparent atmosphere may be summarized by tracing repeated reflections. Solar albedo is then given as

$$\alpha_t = \alpha(\mu_o) + [1 - \alpha(\mu_o)](1 - \alpha_{\text{diff}})\alpha_s\left(\frac{1}{1 - \alpha_{\text{diff}}\alpha_s}\right), \quad (1)$$

where α_s is the underlying surface albedo, α_{diff} is the cloud albedo of the diffuse beam, $\alpha(\mu_o)$ is the cloud albedo of the direct beam, and μ_o is the cosine of the solar zenith angle. This expression yields the concave

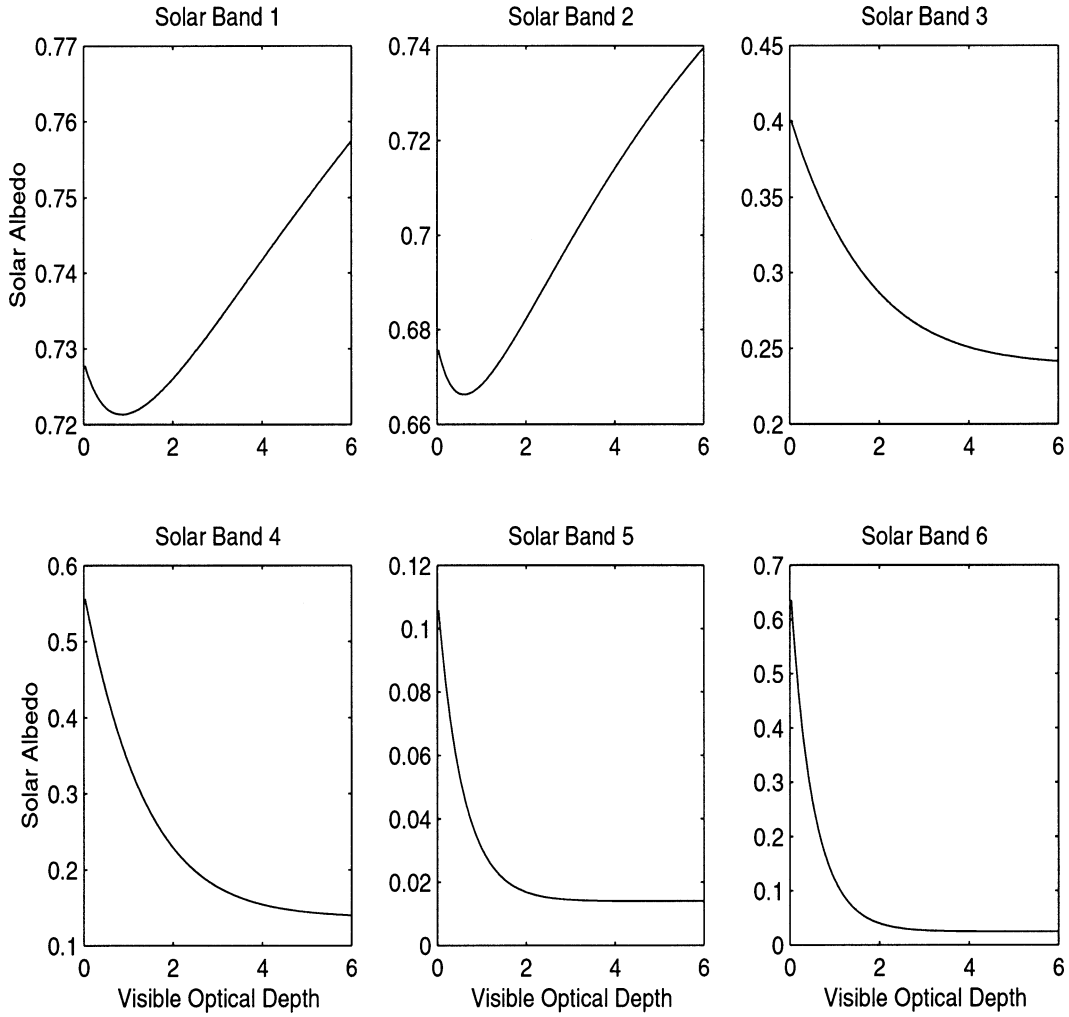

FIG. 2. Solar albedo as a function of high ice cloud optical depth, for each of the six bands in the Fu–Liou radiation model for SZA of 0° and underlying surface albedo of 0.8.

relationship for a highly reflective underlying surface and an overhead sun, so that $\alpha(\mu_o) < \alpha_{\text{diff}}\alpha_s$. Physically, this may be thought of as repeated reflections between the cloud and the surface, while energy is gradually absorbed by the surface. Thus, less energy leaves the top of the atmosphere when a cloud of low optical depth forms over a high reflective surface than for the clear-sky case. Eventually, the cloud becomes thick enough for the direct beam albedo to play the dominant role and the curve reverts to a convex shape.

Throughout this text, low cloud refers to a thick homogeneous water cloud with the liquid water content of 0.2 g m^{-3} located between 1 and 4 km. For this case, as the high cloud thickens, it absorbs more of the photons reflected by the low cloud in the nonconservative scattering bands and the strongly absorbing bands. The reflection in the first two bands of the Fu–Liou radiation model becomes saturated and is not much affected by the changes in thin high-cloud optical depth. The scattering at these wavelengths is dominated by the thick low cloud. Thus, the overall broadband result is a reduced albedo with increased optical depth of the thin high cloud.

A solar albedo bias would not exist if the relationship between solar albedo and cloud optical depth were linear. In scenarios where the relationship exhibits the greatest nonlinearity, the solar albedo bias will be the greatest. The schematic in Fig. 3 shows the case of the convex albedo curve. The PPH result will always be higher than the ICA result. The ICA domain-averaged solar albedo for the cloudy portion of the grid box is given by

$$\alpha_{\text{ica}} = \frac{1}{N}\sum_{n=1}^{N} \alpha_{\text{pph}}(\tau_n), \tag{2}$$

where $\alpha_{\text{pph}}(\tau_n)$ is the plane-parallel homogeneous albedo for a given column. Note that when the albedo–optical depth relationship is concave, the solar albedo would be underestimated by the PPH model, as compared with

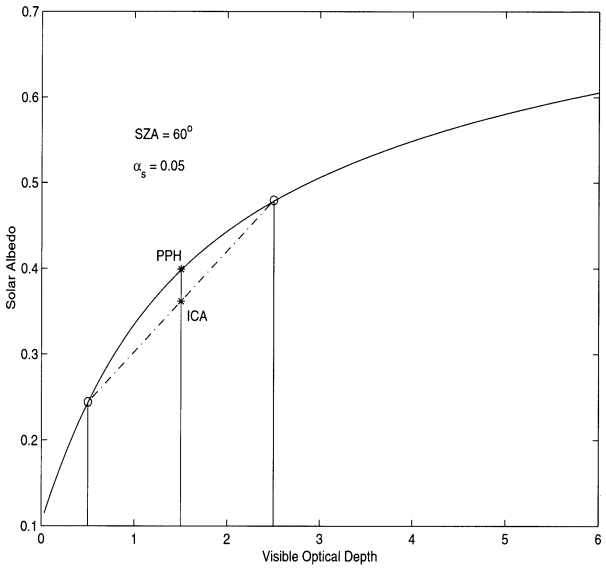

FIG. 3. Demonstration of the PPH bias for an ice cloud in the 9–11-km layer. The PPH result is higher than the ICA result for a scenario where there are two cloud columns of optical depth 0.5 and 2.5. The solid curve shows the results of a PPH calculation.

the ICA. Thus, solar albedo underestimation and overestimation is possible for high clouds under different combinations of solar zenith angle and underlying surface albedo.

It should be noted that for a given cloud system within a GCM grid cell, the error due to using horizontally homogenized clouds in the PPH approach should be evaluated by comparing the PPH and 3D Monte Carlo simulations. This error can be divided into two parts: the difference between the PPH and ICA, and the difference between the ICA and 3D Monte Carlo simulations. Since the ICA uses the exact cloud fields, the difference between the PPH and ICA can be considered as the effects of cloud horizontal inhomogeneity, and the difference between the ICA and 3D Monte Carlo method is caused by the neglect of horizontal photon transport. This study will focus on the former effects. By examining different cloud systems, including tropical mesoscale convective clouds and subtropical stratus clouds, several studies (e.g., Cahalan et al. 1994b; Barker et al. 1999; Fu et al. 2000b) showed that the errors in the ICA are about an order of magnitude smaller than those due to using horizontally homogenized clouds. Note that the ICA has performed extremely well for both stratus clouds (Cahalan et al. 1994b) and towering clouds, along with high anvil clouds (Barker et al. 1999;

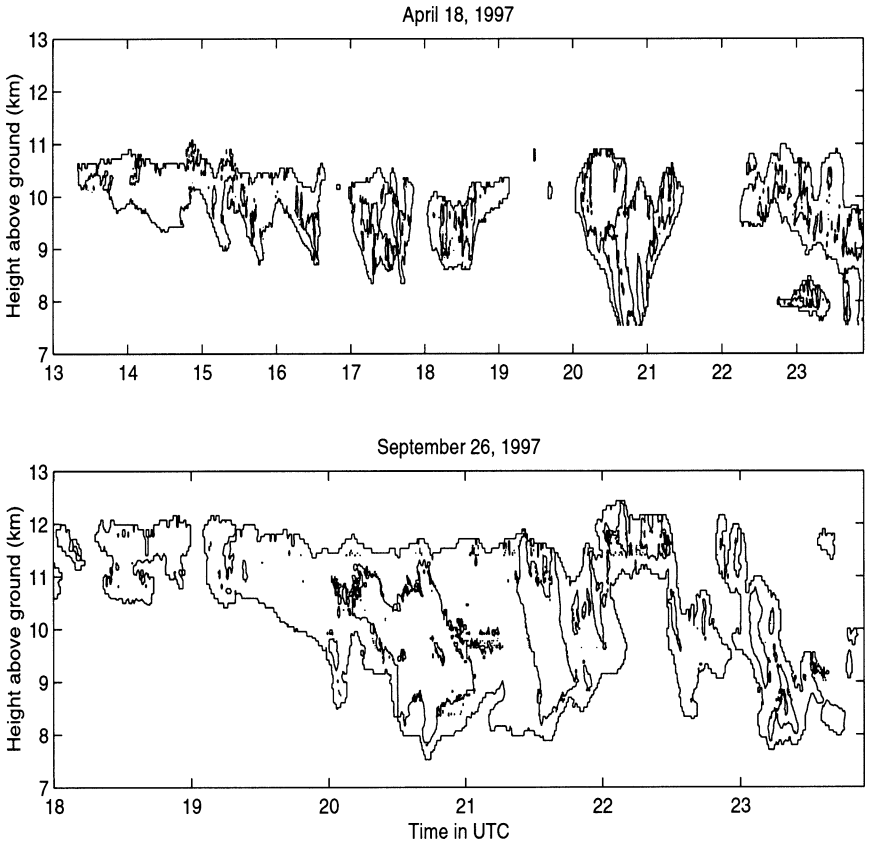

FIG. 4. Contours of the logarithm of IWC (g m^{-3}). Contour lines are −4 and −2.

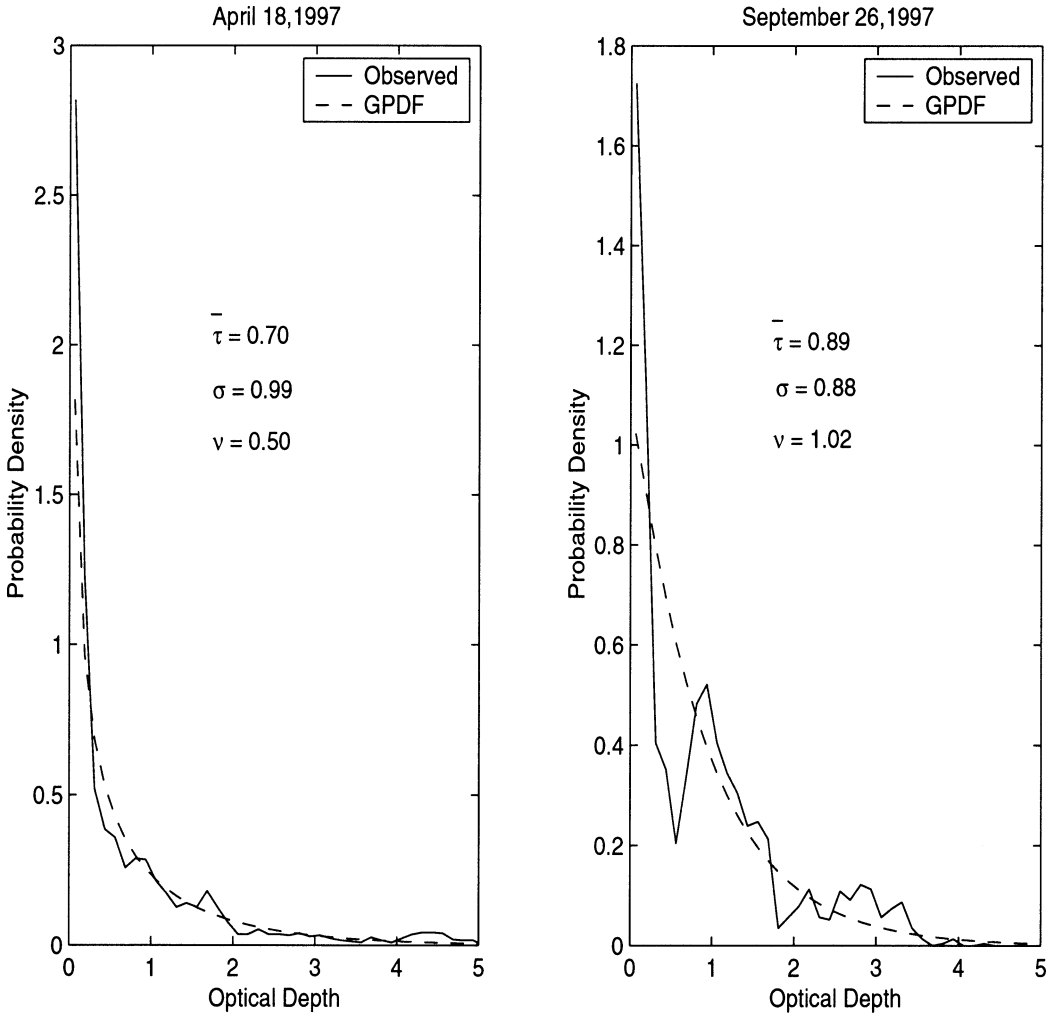

FIG. 5. Optical depth probability density functions for the two MMCR datasets on 18 Apr and 26 Sep 1997.

Fu et al. 2000b). The latter exhibit much larger variability in optical properties than stratus clouds. In any case, the parameterization of horizontal photon transport is beyond the scope of the present study. We consider the difference between the PPH and ICA for the remainder of this study, using the ICA as the reference calculation.

3. Optical depth observations

a. Millimeter cloud radar observations

Spring and fall intensive observation periods (IOPs) were conducted at the Atmospheric Radiation Measurement (ARM) Southern Great Plains (SGP) Cloud and Radiation Testbed (CART) site in Oklahoma during April and September 1997, respectively. High ice cloud data were collected using MMCR on 18 April 1997 and 26 September 1997 for about 10 and 6 h, respectively. Assuming a wind speed between 10 and 20 m s^{-1}, this translates to a spatial scale about the size of a GCM grid box. The MMCR operates at a frequency of 35 GHz, has a wavelength of 8 mm, and a long dwell time (~1 s). The radar uses a low-peak power transmitter (100 W) and a large antenna gain (57.2 dB). This allows for high sensitivity, near −50 dBZ at 5 km, where Z refers to the radar reflectivity factor.

The microphysical properties of the high ice clouds on these dates are derived from an algorithm that uses as input the Doppler moments including radar reflectivity, Doppler velocity, and Doppler velocity variance (G. Mace 2000, personal communication). As the observed Doppler velocity and velocity variance include contributions from the actual particle size distribution as well as from air motions, we need to first separate these two contributions. Following Matrosov et al. (1994), it is assumed that a given temperature and depth within a cloud have similar particle size distributions. The effect of air motions can be accounted for by averaging the Doppler velocity with the assumption that the scatter about the mean is due to turbulent air mo-

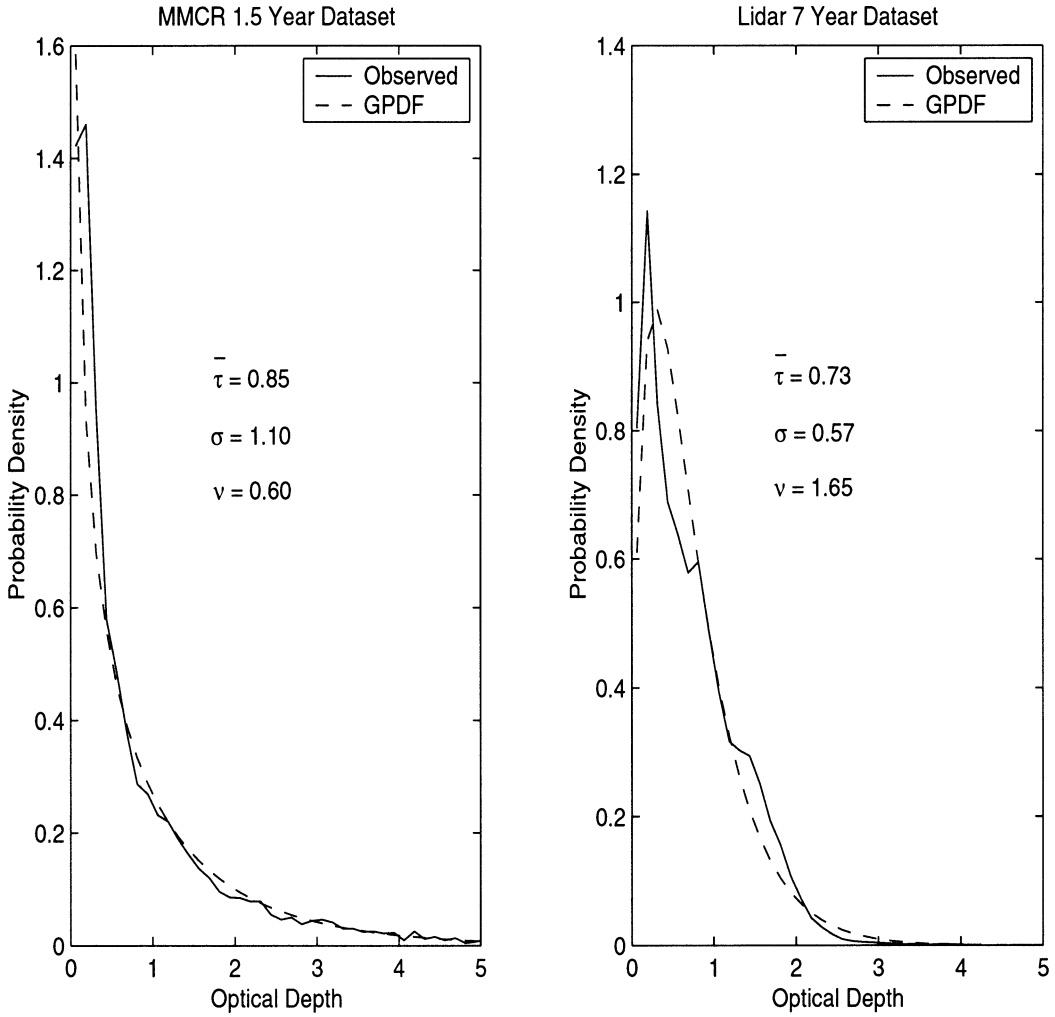

FIG. 6. Optical depth probability density functions for the two compilation datasets.

tions. The effect of turbulent air motions on the Doppler velocity variance have also been considered similarly.

In the retrieval scheme, a bimodal size distribution is used with the large mode represented by a modified gamma function and the small mode by an exponential distribution. The unknowns for these distributions are determined using radar reflectivity, estimated particle fall speed, and velocity variance. The large-particle fall speed is considered to be related to the characteristics of planar polycrystals as in Mitchell (1996). The small particles follow hexagonal crystals as in Heymsfield and Iaquinta (2000). Using the retrieved ice particle size distributions, the ice water content and total cross-sectional area of the ice particles per unit volume can be calculated using mass–length and area–length relations. For the large particle, $m_p = 1.944 \times 10^{-5} L^{2.387}$ and $A_p = 0.304\ L^{1.862}$ where m_p is the particle mass (g), A_p is the cross-sectional area (mm^2), and L is length (mm). For the small particles, we use $m_p = 1.840 \times 10^{-5} L^{2.059}$ and $A_p = 0.197\ L^{1.417}$. The retrieved microphysical properties have been compared with in situ aircraft observations. The University of North Dakota operated the Citation research aircraft equipped with two-dimensional optical probes (2DC and 2DP) for sampling the ice particles. Comparisons of the retrieved results with in situ data show differences of ~50% in ice water content and ~35% in mean particle size. These are comparable with uncertainties found by Matrosov et al. (1994).

The extinction coefficient in the visible spectrum can be calculated following Fu (1996) as

$$\beta = \mathrm{IWC}\left(a_o + \frac{a_1}{D_{ge}}\right), \tag{3}$$

where IWC is ice water content and constant coefficients, a_o and a_1, are -0.29×10^{-4} and 2.52, respectively. The D_{ge} is mean effective size as in Fu (1996):

$$D_{ge} = \frac{2\sqrt{3}}{3}\frac{\mathrm{IWC}}{\rho_i A_c}, \tag{4}$$

where A_c is the total cross-sectional area of ice particles

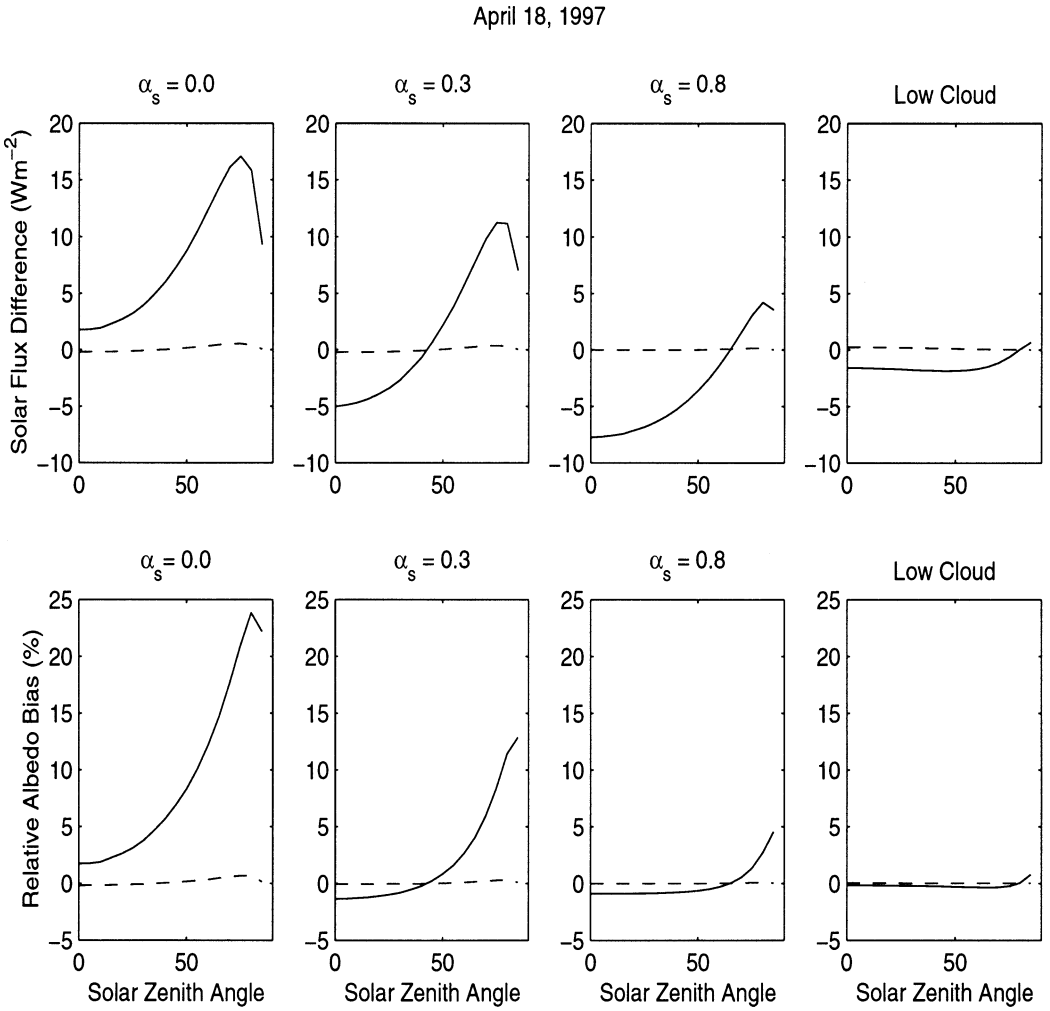

FIG. 7. PPH bias and GWRT error as functions of SZA for underlying surface albedo of 0.0, 0.3, 0.8, and thick low cloud for the 18 Apr 1997 dataset. The PPH bias is given by the solid line and the GWRT error is given by the dashed line.

per unit volume and ρ_i is the pure ice density (925 kg m^{-3}). The cloud optical depth is then found by vertical integration through the cloud:

$$\tau = \int_{z_b}^{z_t} \beta(z)\, dz, \tag{5}$$

where z_t and z_b are the cloud-top and -base heights, respectively.

A vertical cloud column is available averaged over 10 s following this retrieval algorithm. Figure 4 shows the retrieved IWC on 18 April 1997 and 26 September 1997. The ice clouds are located between 8 and 12 km with ice water contents in the range between 10^{-4} and 10^{-2} g m^{-3}. The retrieved optical depth probability density function is shown in Fig. 5 for the same two cases. There were 2388 and 1841 retrievals of optical depth for the two cases, respectively. A gamma probability density function was used to fit the observed distributions. This is also shown in Fig. 5. The gamma probability density function $P_\Gamma(\tau)$ (Barker and Fu 2000) is

$$P_\Gamma(\tau) = \frac{1}{\Gamma(\tau)}\left(\frac{\nu}{\overline{\tau}}\right)^{\nu} \tau^{\nu-1} e^{-\tau\nu/\overline{\tau}}, \tag{6}$$

where the two parameters are mean optical depth, $\overline{\tau}$, and ν. The parameter ν is given by the methods of moments (MoM) as

$$\nu = \left(\frac{\overline{\tau}}{\sigma}\right)^2, \tag{7}$$

where σ is the standard deviation of optical depth. The degree of variability is then characterized by the parameter ν. As ν approaches zero, the dataset may be thought of as being increasingly inhomogeneous. As ν goes to infinity, the set is increasingly homogeneous. The values for the parameters $\overline{\tau}$, σ, and ν are shown in Fig. 5. The mean cloud optical depths for the 18 April and 26 Sep-

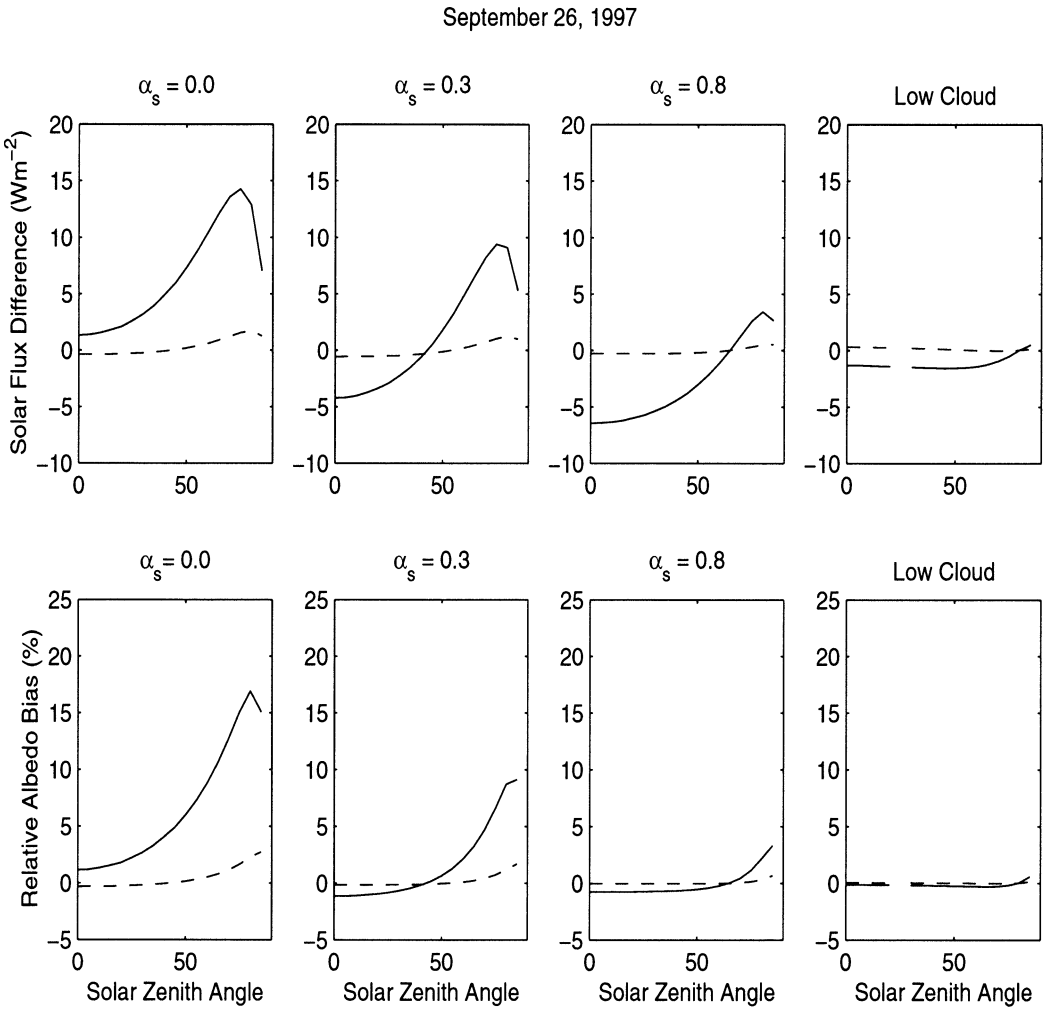

FIG. 8. Same as Fig. 7, but for 26 Sep 1997 dataset.

tember cases were 0.70 and 0.89, respectively. The standard deviations of optical depth were 0.99 and 0.88, respectively, with resulting ν values of 0.50 and 1.02. We can see that the ice clouds of 8 April are horizontally more inhomogeneous than those of 26 September.

Another reasonable way to compute ν is by maximum likelihood estimation (MLE). This involves solving the equation

$$\frac{d\ \ln\Gamma(\nu)}{d\nu} + \ln\left(\frac{\overline{\tau}}{\nu}\right) - \overline{\ln\tau} = 0. \tag{8}$$

The MLE ν values were 0.66 and 0.87 for the 18 April and 26 September cases, respectively. The PPH bias was found to be not overly sensitive to the method of computing ν for these clouds. Solar flux differences were less than 1 W m^{-2} between the MoM and MLE ν. Thus, MoM estimates of ν are used for all radiative calculations presented.

The third MMCR dataset is a compilation of 6803 observations of high-cloud optical depth retrieved at the ARM SGP CART site between 8 November 1996 and 31 May 1998 following the MMCR algorithm as in Mace et al. (1998). This retrieval algorithm uses infrared radiance spectra observed by Atmospheric Emittance Radiance Interferometer (AERI; Smith et al. 1993) combined with radar reflectivity observation in order to derive the microphysical properties of ice cloud layers. The particle size distribution is assumed to be entirely described using a modified gamma function. The unknown parameters of the distribution are determined from the observed downwelling radiance and the radar reflectivity as outlined in Mace et al. (1998). Note that this retrieval is formulated in terms of spherical particles. Mace et al. (1998) demonstrate good agreement of retrieved results with in situ data. This retrieval provided the optical depth of a vertical cloud column every 10 min and is thus at considerably coarser resolution than the two IOPs. While this dataset does not exactly represent a cloud as in one GCM grid box, it is of interest to compare the statistical properties at this spatial and temporal scale to the previous two cases, which do rep-

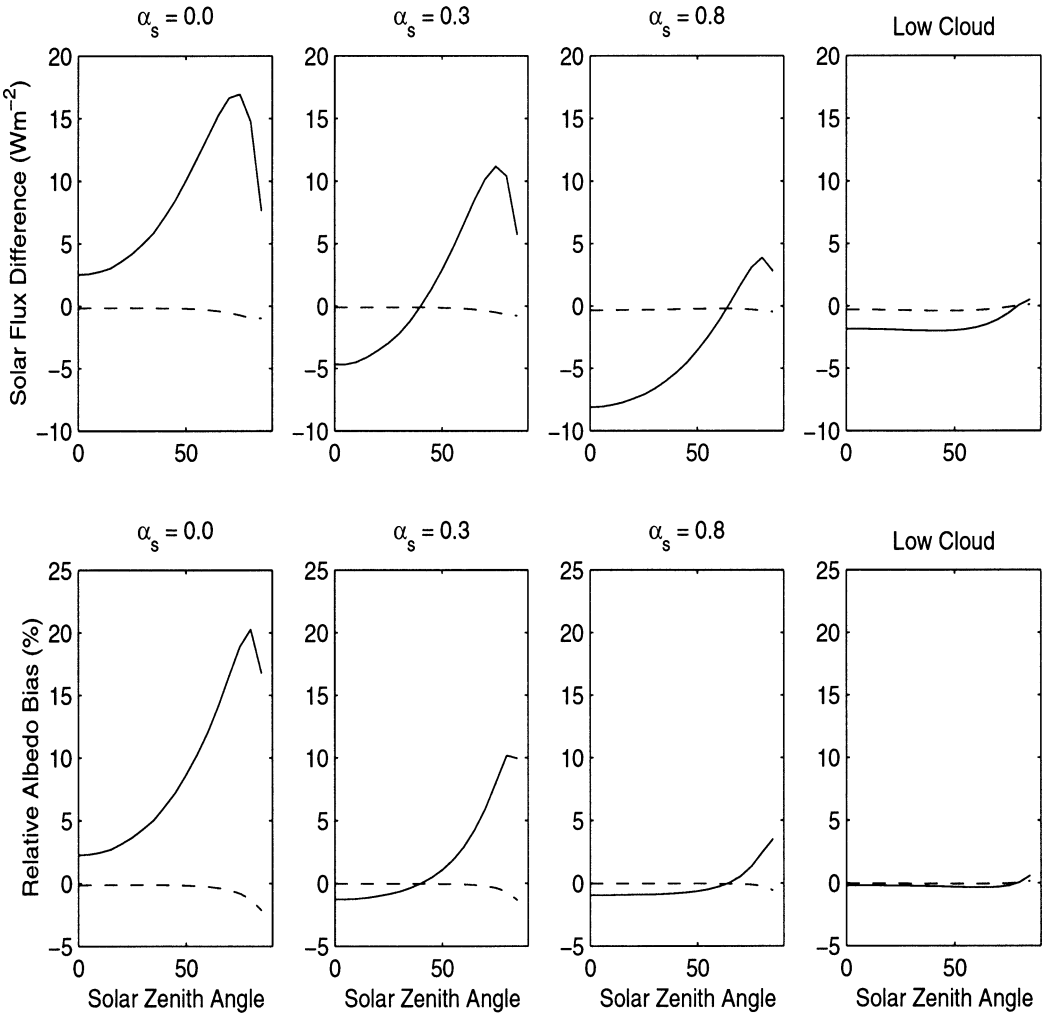

FIG. 9. Same as Fig. 7, but for MMCR compilation.

resent a GCM grid box. We see a definite similarity in comparing Fig. 5 and Fig. 6a. Figure 6a shows the probability density and the gamma fit for the MMCR compilation. The mean cloud optical depth, standard deviation of optical depth, and ν were found to be 0.85, 1.10, and 0.60, respectively.

b. Lidar observations

The final dataset is a lidar compilation. Optical depth was retrieved using the Facility for Atmospheric Remote Sensing (FARS) Cloud Polarization Lidar (CPL) at the University of Utah located in Salt Lake City, Utah. The CPL is a dual-channel polarization ruby lidar that operates at a wavelength of 0.694 μm. The maximum pulse repetition frequency is 0.1 Hz and transmits a 1–3-mrad beamwidth pulse that is vertically polarized. Further detail concerning FARS instrumentation and measurement philosophy is provided in Sassen et al. (2001). The CPL is combined with a narrow beam midinfrared radiometer (9.25–12.0 μm) for the retrieval of visible optical depth at the lidar wavelength.

The use of combined lidar and radiometric measurements (LIRAD) to study cirrus clouds dates back to the early 1970s (Platt 1973). The lidar derived cirrus optical depths used in this study were estimated using a retrieval scheme that is based on the LIRAD technique with some modifications, as described in Comstock and Sassen (2001). Cirrus cloud optical depth was retrieved using 2-min averages of lidar and radiometric data, which resulted in 23 793 retrievals between 22 April 1992 and 28 February 1999. The dataset includes a combination of midlatitude cirrus types (synoptic, anvil, and orographic). A detailed analysis of the radiative properties derived from FARS measurements during this time period is presented in Sassen and Comstock (2001).

Like the third dataset, this one does not represent a single GCM grid box. However, it is of interest to examine the statistical properties at this spatial and temporal scale. We note that this dataset is not highly dis-

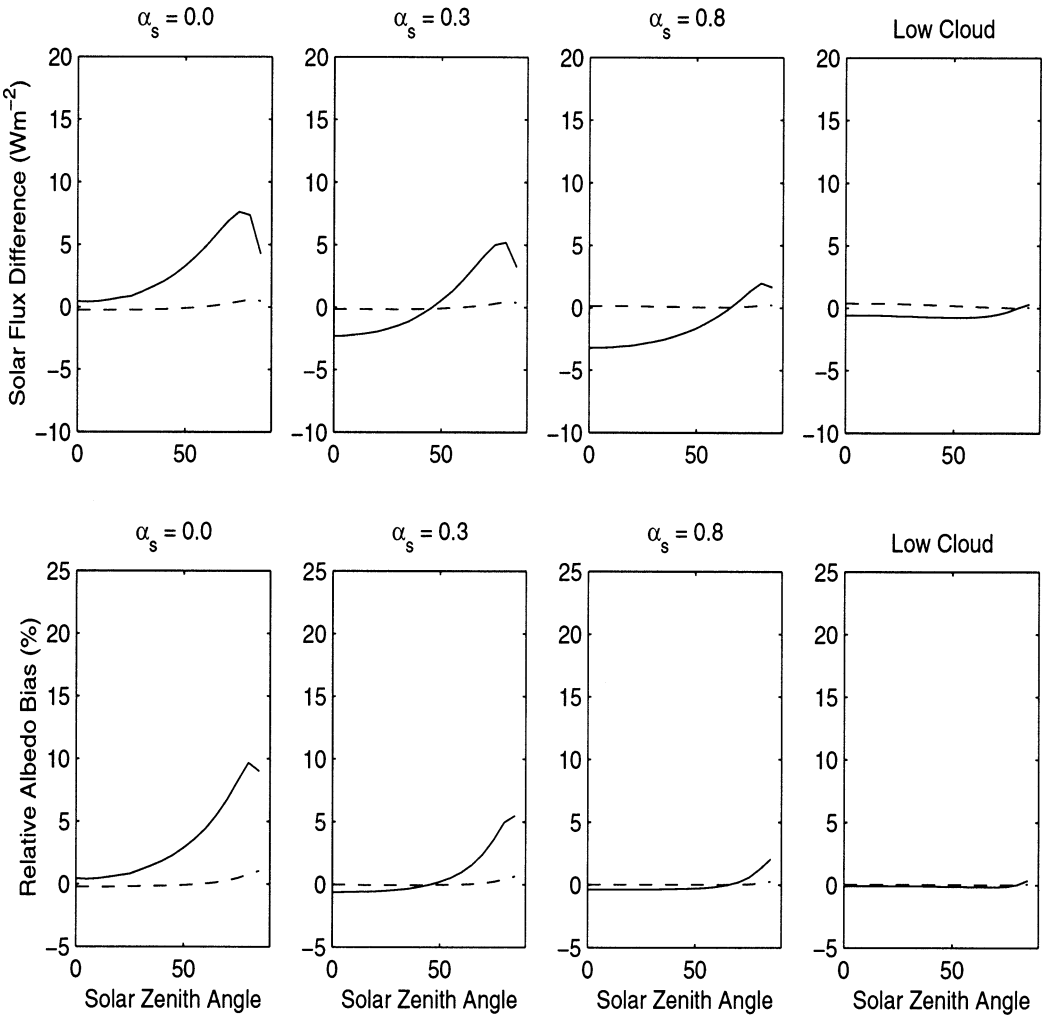

FIG. 10. Same as Fig. 7, but for lidar compilation.

similar from the first two cases, which do represent a GCM grid box exactly. The optical depth probability density function for this dataset is summarized in Fig. 6b. The mean cloud optical depth was found to be 0.73. The standard deviation of optical depth was 0.57, and the resultant value of the parameter ν was 1.65. Note that the standard deviation for the lidar dataset is smaller than those derived from MMCR datasets. This difference might be mainly because the FARS data are only for cirrus, which has an optical depth smaller than 3, while the MMCR data include both cirrus and thicker high clouds (Sassen 2001). It should be also noted that since radar reflectivity is proportional to the sixth power of the particle size, the MMCR might miss thin cirrus and underestimate cloud-top heights and thicknesses. On the other hand, lidars might miss the upper portions of dense ice clouds due to the effects of optical attenuation.

TABLE 1. Spherical albedo is shown followed in parenthesis by the percent bias/error relative to the ICA for a surface albedo of 0.0. Datasets 1 and 2 are the two MMCR IOPs on 18 Apr and 26 Sep 1997, respectively. Datasets 3 and 4 are the compilations for the 1.5-yr MMCR and 7-yr lidar, respectively.

Dataset no.	$\overline{R}_{\mathrm{ICA}}$	$\overline{R}_{\mathrm{PPH}}$	$\overline{R}_{\mathrm{GWRT}}$
1	0.1274	0.1415 (+11.07)	0.1277 (+0.24)
2	0.1468	0.1585 (+07.97)	0.1477 (−0.61)
3	0.1397	0.1546 (+10.67)	0.1392 (−0.36)
4	0.1382	0.1440 (+04.20)	0.1383 (+0.07)

4. Solar albedo bias estimates and correction

We apply the Fu–Liou radiation model to perform an ICA for each of the four datasets. Domain-averaged solar albedo is then determined as in Eq. (2). Note that throughout this study we consider radiative transfer involving only the cloudy portion of the grid box. In parallel, we take the mean optical depth for each dataset and use this to perform a PPH calculation. This is similar

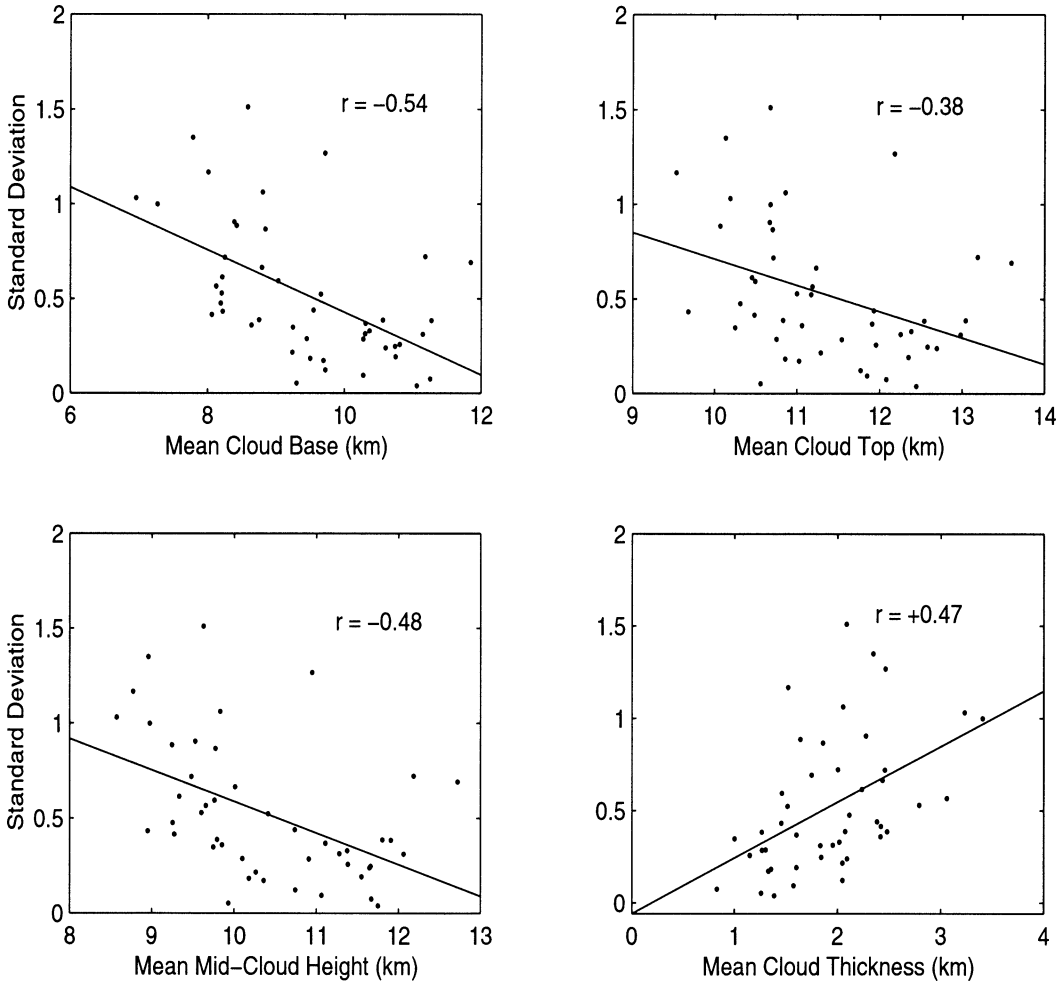

FIG. 11. Single-variable correlations between the standard deviation of optical depth and GCM known domain-averaged variables including mean cloud base, mean cloud top, mean midcloud height, and mean cloud thickness.

to what a GCM would do. The solar albedo bias is the PPH result minus the ICA result. We also calculate solar albedo by applying the gamma-weighting correction method of Barker et al. (1996). The gamma-weighted solar albedo is

$$\alpha_\Gamma = \int_0^\infty P_\Gamma(\tau)\alpha_{\text{pph}}(\tau)\, d\tau. \tag{9}$$

The GWRT error is found in comparison with the ICA result. The PPH bias and GWRT error are presented in Figs. 7–10 as a function of solar zenith angle (SZA) using different underlying surface albedo scenarios for the two IOPs and two compilations.

The solar albedo bias generally increases with SZA, up to $\overline{\tau}/\mu_o$ of about 5, where μ_o is the cosine of solar zenith angle. This is a consequence of the increasingly convex shape of the albedo function. Cloud horizontal inhomogeneity plays a greater role with the longer path-lengths through the cloud at higher SZA. The negative albedo bias is seen, as expected, for the overhead sun and highly reflective underlying surface scenarios. The bias is not as negative when a low cloud underlies the thin high cloud. The nonlinearity between high-cloud

TABLE 2. Same as Table 1, but for a surface albedo of 0.3.

Dataset no.	$\overline{R}_{\text{ICA}}$	$\overline{R}_{\text{PPH}}$	$\overline{R}_{\text{GWRT}}$
1	0.3051	0.3109 (+1.90)	0.3052 (+0.03)
2	0.3151	0.3199 (+1.52)	0.3154 (+0.10)
3	0.3116	0.3178 (+1.99)	0.3112 (−0.13)
4	0.3099	0.3122 (+0.74)	0.3099 (+0.00)

TABLE 3. Same as Table 1, but for a surface albedo of 0.8.

Dataset no.	$\overline{R}_{\text{ICA}}$	$\overline{R}_{\text{PPH}}$	$\overline{R}_{\text{GWRT}}$
1	0.6385	0.6363 (−0.34)	0.6386 (+0.02)
2	0.6372	0.6252 (−0.30)	0.6372 (+0.00)
3	0.6378	0.6355 (−0.36)	0.6375 (−0.05)
4	0.6362	0.6362 (−0.14)	0.6373 (+0.03)

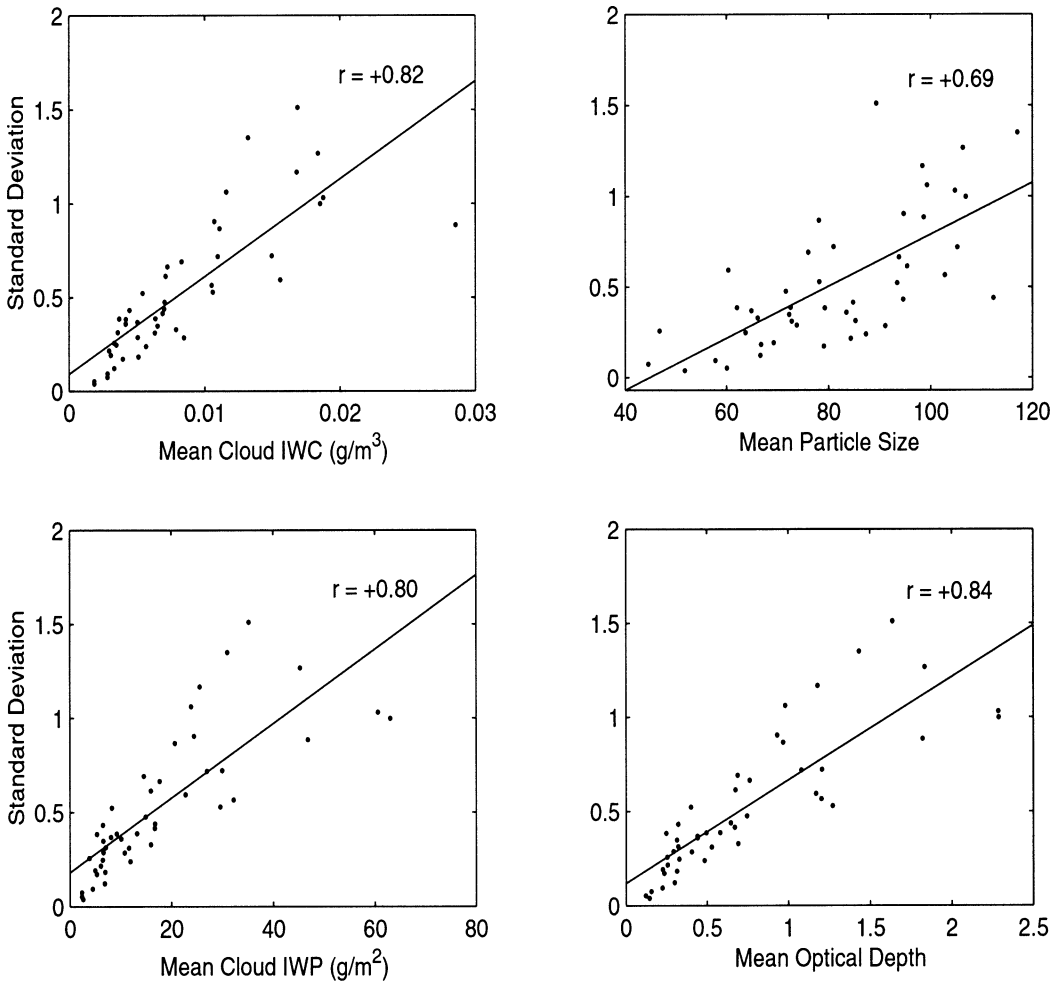

FIG. 12. Same as Fig. 11, but for the domain-averaged variables including mean cloud IWC, mean particle size, mean cloud IWP, and mean cloud optical depth.

optical depth and albedo is not as great in that case. The maximum relative solar albedo bias was about 25%. This occurred for the 18 April 1997 dataset, when placed over a low reflective surface. This case is characterized by the highest value of ν and is the most inhomogeneous. The relative solar albedo bias is found to be as high as 20% for the MMCR compilation and 10% for the lidar, both over the low reflective surface. Note that the compilations, unlike the two IOP cases, will not exactly represent the PPH bias in one GCM grid box. However, despite the different spatial and temporal resolution, there is a similarity in the PPH bias between all the MMCR datasets. The lidar may tend to underestimate the bias because this dataset is limited to only cirrus clouds (optical depth of 3 and less).

We note that the GWRT gives the outgoing solar flux

TABLE 4. Multiple correlation coefficient squared (R^2). The correlation is between standard deviation of optical depth and the two independent variables as shown on the row and column. Note that all variables referred to are mean values for each cloud system.

	IWC	Cloud height	Optical depth	Particle size	Cloud top	Cloud base	Cloud thickness	IWP
IWC	0.666	0.680	0.722	0.739	0.672	0.688	0.691	0.685
Cloud height	0.680	0.234	0.718	0.501	0.337	0.337	0.337	0.644
Optical depth	0.722	0.718	0.712	0.756	0.722	0.714	0.727	0.795
Particle size	0.739	0.501	0.756	0.482	0.495	0.504	0.488	0.686
Cloud top	0.672	0.337	0.722	0.495	0.145	0.337	0.337	0.649
Cloud base	0.688	0.337	0.714	0.504	0.337	0.295	0.337	0.636
Cloud thickness	0.691	0.337	0.727	0.488	0.337	0.337	0.225	0.645
IWP	0.685	0.644	0.795	0.686	0.649	0.639	0.645	0.632

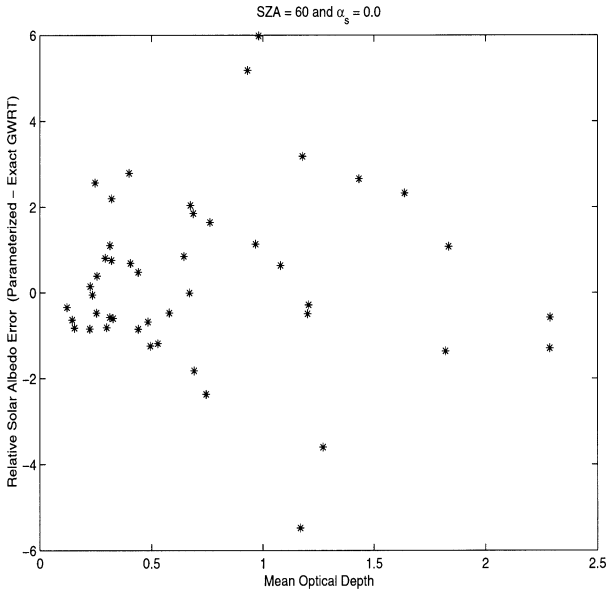

FIG. 13. Relative solar albedo error (%) in the GWRT using the multivariable regression model given by Eq. (11) compared to GWRT using the exact standard deviation, for the 46 cloud fields of the MMCR dataset.

to within 1 W m^{-2} of the ICA in all scenarios except for 26 September 1997 at high SZA. Even in this worst scenario, the bias is within 2 W m^{-2} of the ICA. This demonstrates that the GWRT is an effective method of solar albedo bias correction suitable for GCM application. The GWRT worked well for all distributions, including the IOP cases, which represent a GCM grid box, and the compilations, which were at a different spatial/temporal scale. The CPU time is increased by only 25% when the GWRT is applied (Barker and Fu 2000). This may be well worth the expense as the conventional two stream approximation usually accounts for less than 1% of the typical GCM CPU time (Barker 1996b).

To summarize the solar albedo bias on a daily averaged basis, we calculate spherical albedo. Spherical albedo is

$$\alpha_{\text{sph}} = 2 \int_0^1 \alpha \mu_o \, d\mu_o, \tag{10}$$

where α is the domain-averaged solar albedo, which may be found by the ICA, PPH, or GWRT methods, and μ_o is the cosine of solar zenith angle. Spherical albedo is calculated for each of the four datasets using three underlying surface albedo values of 0.0, 0.3, and 0.8, with the ICA, PPH, and GWRT methods. These results are presented in Tables 1–3. We note that the relative spherical albedo bias is as high as 11% over the low reflective surface on 18 April 1997. The relative bias is minimal over the high reflective surface (less than 1% in all cases) and is a consequence of the cancellation of the albedo bias between the high and low solar zenith angles. This bias is negligible with an underlying low cloud and is not shown. The GWRT error is always less than 1% for all scenarios. The highest GWRT error is over the low reflective surface for 26 September 1997. This probability density function had a trimodal appearance, which the gamma probability density function can not capture. Thus, the error is greater. Overall, the GWRT has been demonstrated to be extremely effective at correcting the solar albedo bias. It should be noted here that while solar albedo has been used to illustrate the method, it is equally valid to use either transmittance or absorptance (Cahalan et al. 1994b; Barker 1996a).

5. Predicting the standard deviation of high-cloud optical depth

In order to minimize the solar albedo bias in any radiative transfer scheme, cloud subgrid-scale variability in optical depth must be parameterized. Currently, a GCM predicts mean cloud optical depth but not the standard deviation of optical depth, or any other parameter associated with subgrid-scale variability. In order for GWRT to be applied in a GCM, we must find some relation between the standard deviation of optical depth and known domain-averaged GCM variables. Certainly characterizing subgrid-scale variability is a daunting task. We use the MMCR compilation dataset to proceed with single variable and multivariable correlations between the standard deviation of optical depth and variables known within a GCM framework. We are using the radar dataset because it is unique for our purposes. This dataset includes cloud-top, -base, and midcloud heights and quantities derived with supplemental data from IR radiometer including optical depth, particle size, and ice water content. The dataset is divided into separate cloud fields. When one hour or more elapses between retrievals, a separate cloud field is created. Cloud fields with less than 30 optical depth retrievals contained therein are removed from the dataset. Following this process, 46 separate cloud fields remained in the study.

a. Single-variable correlations

We have correlated the standard deviation of optical depth with the following domain-averaged quantities, all of which are available in a GCM: cloud-base and -top heights, midcloud height, cloud thickness, ice-water content, particle size, ice water path (IWP), and cloud optical depth. Unfortunately, cloud fraction was not available for this dataset. This is another potential independent variable, which may be used to model ν (Barker et al. 1996) or the variance of optical depth (Oreopoulos and Davies 1998b). Note that here we assumed the grid-cell size is such that it is filled with the whole single cirrus cloud system. But if not, a more generalized approach that divides the dataset using dif-

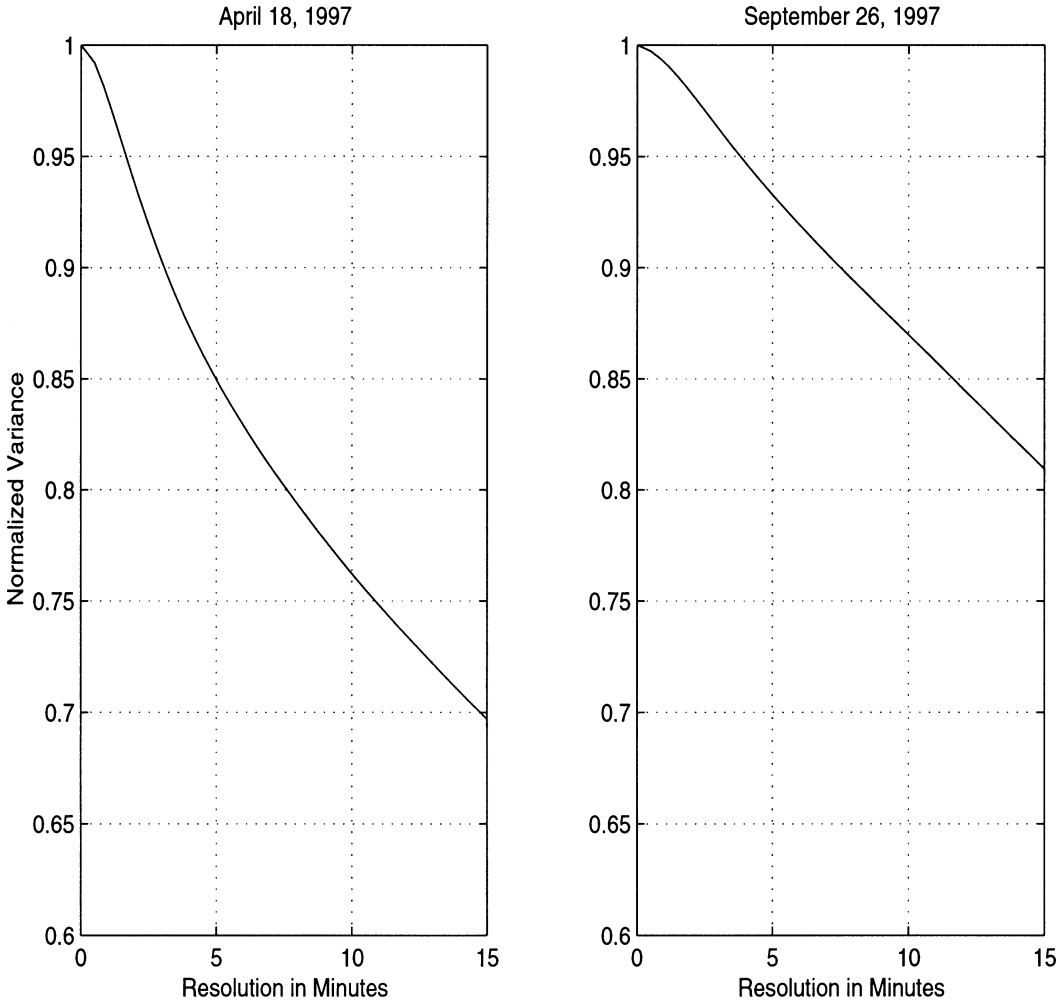

FIG. 14. Variance of optical depth as found at varied resolution normalized by the 10-s value.

ferent time intervals such as 1, 3, 6, and 12 h should be used so that the parameterization can be developed for clouds at different spatial scales (Pomroy and Illingworth 2000).

Scatterplots relating the standard deviation of cloud optical depth with the above noted variables and least square line fits are shown in Figs. 11 and 12. Each point represents a separate cloud field. The highest correlation was with domain-averaged optical depth. The correlation coefficient was 0.84. The value of the correlation coefficient squared tells us the proportion of the standard deviation of optical depth that can be accounted for by the variable in question. For example, 71% of the standard deviation of optical depth can be accounted for by knowledge of the mean optical depth.

High clouds with greater mean optical depth appear to have a higher standard deviation of optical depth (i.e., greater inhomogeneity). Physically, this might occur because optically thicker high clouds might be associated with greater mesoscale convection. Greater mesoscale convection would lead to a larger updraft and downdraft, which then produces greater horizontal inhomogeneity. A similar argument could be proposed for the correlation seen with IWC and IWP, and geometric cloud thickness. It also appears that the highest clouds are more homogeneous. This might be a result of there being less convection at higher levels. Further research is needed to examine single-variable correlations for other long-term datasets.

b. Multivariable regression

We next examine the multiple correlation coefficient squared, relating pairs of independent variables to the standard deviation of optical depth. These results are summarized in Table 4. The best result is for the combination of domain-averaged optical depth and IWP. Here we see that 80% of the standard deviation of optical depth can be accounted for by these two variables. This suggests a parameterization for standard deviation in the form

$$\sigma = c_1 + c_2\overline{\tau} + c_3\overline{\mathrm{IWP}}, \tag{11}$$

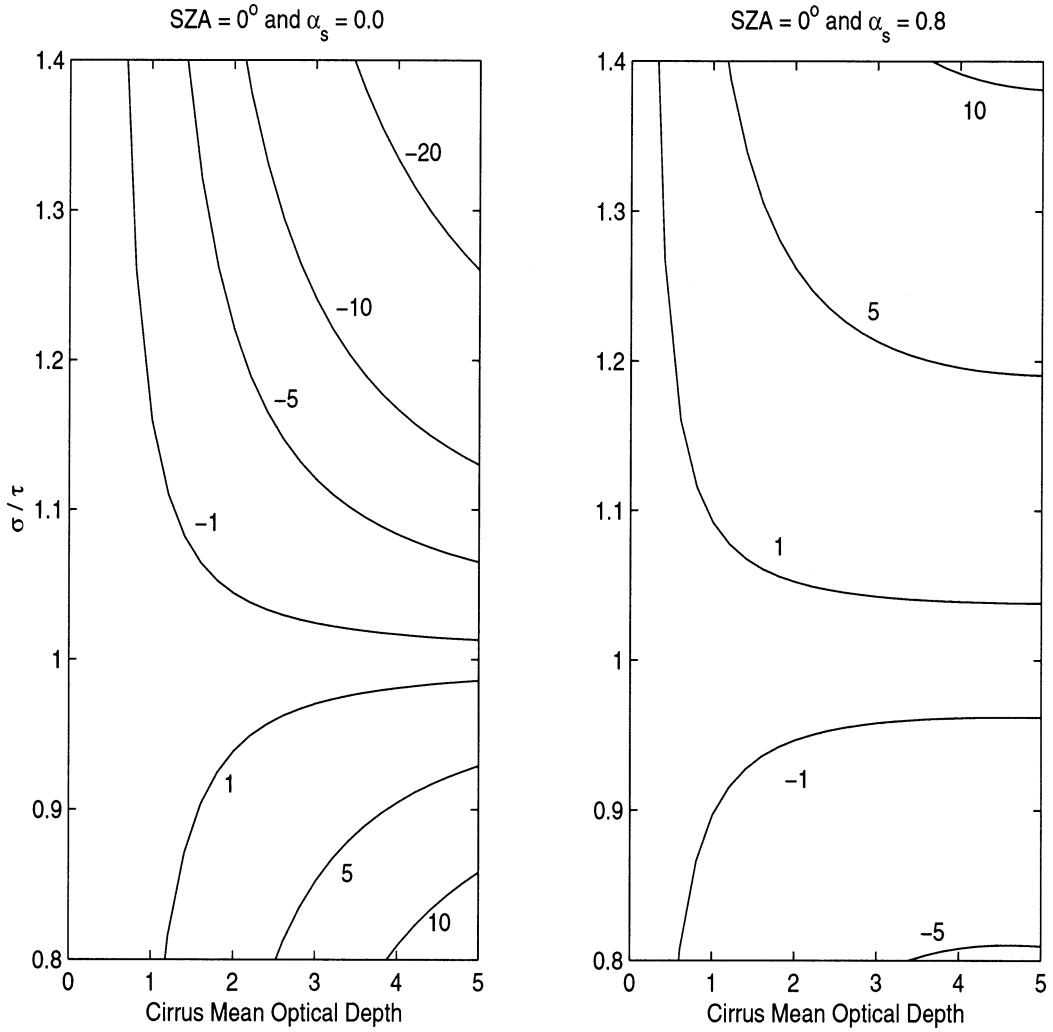

FIG. 15. Contours of outgoing solar flux error (W m^{-2}), comparing GWRT flux using ν of one and GWRT flux using a range of ν values based on the relation between standard deviation and mean optical depth shown on the vertical axis. This is shown for a solar zenith angle of 0° and underlying surface albedos of 0.0 and 0.8.

where the c parameters refer to constants. Multivariable regression was applied to the 46 cloud fields from the MMCR dataset to produce a model as in Eq. (11). In the case of a solar zenith angle of 60° and surface albedo of 0.0, Fig. 13 shows the relative solar albedo error of the GWRT using this model as compared to the GWRT using the exact standard deviation. For about 90% of the cloud fields, the error was less than 3%. This is a considerable improvement over the PPH bias.

Recall that we often relate optical depth and IWP as

$$\tau = c_4 \frac{\text{IWP}}{D_{ge}}. \tag{12}$$

We can then substitute Eqs. (11) and (12) into Eq. (7), assuming c_1 is small, to obtain

$$\nu = \left(\frac{1}{c_2 + c_5 \overline{D_{ge}}} \right)^2. \tag{13}$$

Thus, the parameter of the gamma distribution may be parameterized only in terms of the mean particle size when c_1 is small.

We have compared the error in using the single-variable model, as compared to the multivariable model, as applied to each of the 46 cloud fields to predict the standard deviation of optical depth (not shown). In the majority of cases the error is less with the multivariable model. Thus, we suggest that a multivariable parameterization of the standard deviation of optical depth based on IWP and optical depth would be the most accurate model. However, these preliminary results also suggest that if one chooses to instead parameterize ν, a

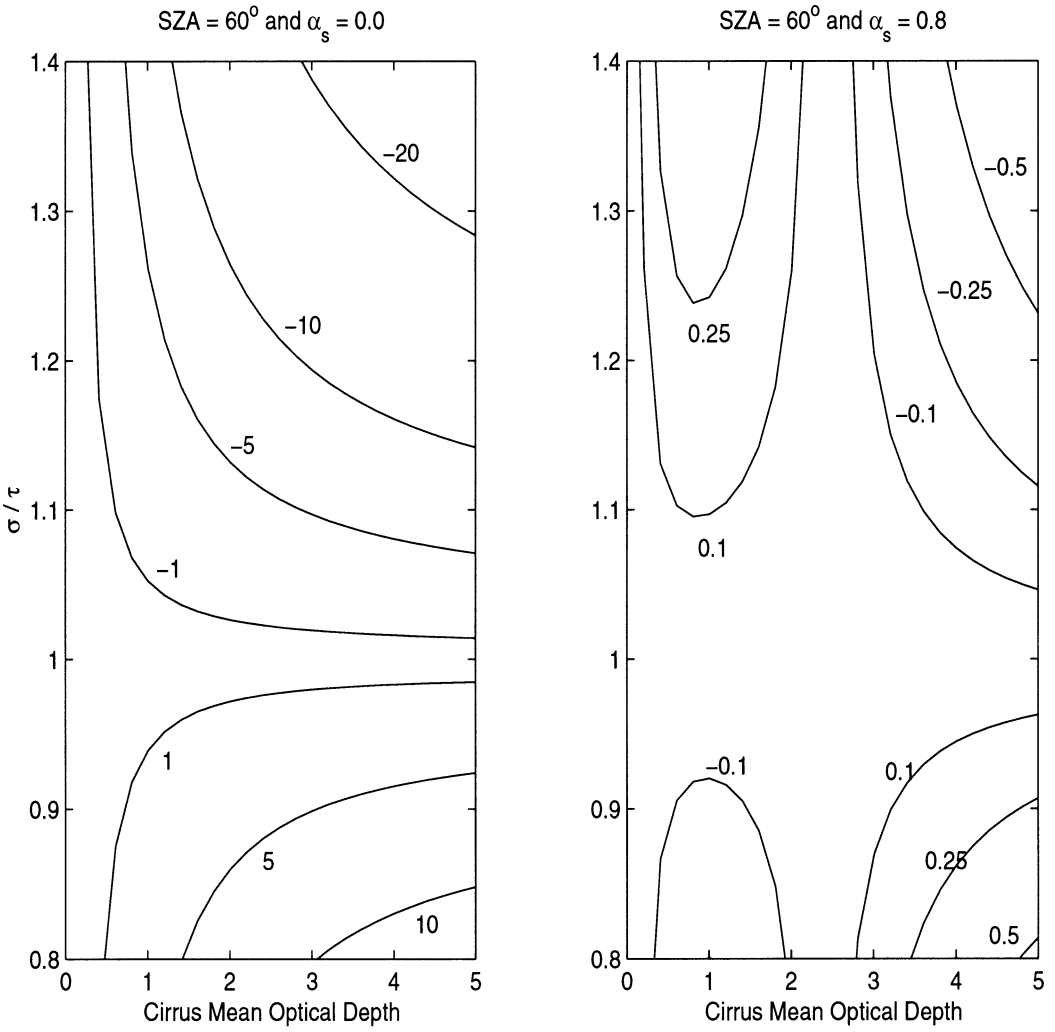

FIG. 16. Same as Fig. 15, but for solar zenith angle of 60° and underlying surface albedos of 0.0 and 0.8.

single variable with a second power relation may prove sufficient. Further investigation is needed using more long-term high-resolution cloud field datasets.

c. Resolution for an accurate parameterization

The question arises, how fine a resolution must we measure optical depth to arrive at a sound parameterization? Recall that for the MMCR 18 April 1997 and 26 September 1997 datasets, we have an optical depth retrieval every 10 s. If we assume that the high cloud is passing above the instrument with the average wind speed of 20 m s^{-1}, this means that we have observed the cloud at a spatial resolution of 200 m. Figure 14 shows how the variance changes with progressively coarser resolution up to sampling only once every 15 min. The percentage drop in variance, defined as σ^2, reflects the loss of information. For the 18 April 1997 case, we have lost 30% of the information by sampling once every 15 min. The curve appears to plateau for sampling times below 1 min. This suggests that a resolution of 1 min. or less would be useful to arrive at a sound parameterization. We suggest at this time that it is necessary to further examine high-cloud horizontal inhomogeneity at such high resolution over more datasets.

For computational efficiency, it has been suggested that an integer value of the parameter ν be used when the GWRT scheme is employed (Barker and Fu 2000). If this were to be the case, then perhaps also a simpler parameterization such as assigning a fixed value to ν for a certain cloud type or cloud type associated with its fractional coverage of the grid box would suffice. For these midlatitude datasets, the ν value rounds to 1 for the three MMCR datasets and to 2 for the lidar dataset. Note that the lidar dataset was exclusively for cirrus clouds while the MMCR also included other high ice cloud types. Further research is needed to examine if a characteristic ν can be found for different cloud types or perhaps for cloud type associated with fractional cloud coverage.

To consider the error incurred by assuming ν is an integer, we present Figs. 15 and 16. These figures show contours of the difference in outgoing solar flux between GWRT using ν of one and GWRT using a range of ν values as shown on the vertical axis, and for different combinations of solar zenith angle and underlying surface albedo. The error increases with mean optical depth. These results suggest that using an integer for a certain cloud type may not be a satisfactory correction, particularly for thicker high clouds.

6. Conclusions

This study has examined the effect of high ice cloud horizontal inhomogeneity on the reflected solar radiation using four midlatitude datasets. The MMCR datasets from 18 April 1997 and 26 September 1997, had mean cloud optical depths of 0.70 and 0.89, with standard deviations of optical depth of 0.99 and 0.88, respectively. Two compilation datasets, over 1.5 yr from MMCR, and over 7 yr from lidar, were also presented. The mean optical depths for these two compilations were 0.85 and 0.73, with standard deviations of 1.10 and 0.57, respectively. The parameter ν required by the GWRT scheme was found to be 0.50, 1.02, 0.60, and 1.65 for these four midlatitude datasets, respectively. The parameter ν was similar in the first three datasets, derived from MMCR, despite the fact that two cover an approximately 6-h period and one covers a period of years.

It is important to note that the lidar dataset represents true cirrus exclusively and does show less variability than the clouds detected by the MMCR. The MMCR datasets include other optically thicker high clouds, which may be characteristically more variable as they are deeper and more active. We also note that these datasets have been limited to midlatitude high clouds. In different regions it is expected that there may be differences in high-cloud properties. Further observation needs to be conducted on high clouds in both the Tropics and at higher latitudes. Tropical cirrus may, in some cases, be associated with deep convection and might therefore exhibit greater horizontal inhomogeneity than the typical midlatitude cirrus. However, tropical cirrus may, in other cases, be quite high and subvisible, possibly more homogeneous.

We have demonstrated a relative solar albedo bias up to 25% using the MMCR datasets and up to 10% using the lidar dataset. A relative spherical solar albedo bias up to 11% was found for the MMCR, and slightly over 4% for the lidar. This solar albedo bias would be significant in a PPH model, considering that global high-cloud cover is at least 20% (Hartmann et al. 1992). This depends on how high cloud is defined, which is an issue of importance in comparison of model results and observations. A better consensus should be reached on how much cloud is included when reference is made to mean optical depth, its variance, and cloud fraction.

The GWRT scheme was shown to be an effective method of correction, with an error less than 1 W m^{-2}. We have used the method of moments fit to determine the parameter of the gamma probability density function. The method of moments fit has been suggested as the best fit for single-layer cloud cases such as we have examined here (Barker et al. 1996). Further studies of high clouds overlying other cloud layers are needed. This becomes a more difficult issue given the need for a cloud overlap treatment.

We suggest that the standard deviation of optical depth may be parameterized with a multivariable model using ice water path and optical depth. This would be one approach to characterizing the cloud subgrid-scale variability. Another approach would be to parameterize the parameter, ν, required by the gamma probability density function. This may be done using only the domain-averaged particle size. We note that additional datasets need to be examined at high resolution over long sampling periods to arrive at a sound parameterization.

GCM cloud–radiation feedback cannot be accurate without a sound parameterization of cloud subgrid-scale variability in optical depth. We have shown that neglect of high-cloud horizontal inhomogeneity leads to solar albedo overestimation over a low reflective surface. Solar albedo underestimation may occur over a high reflective surface. The majority of the earth's surface is water covered, and thus, low reflective. In the global mean, this suggests that GCMs reflect too much solar energy back to space. Thus, the magnitude of the shortwave cloud forcing may not be as large when a correction such as the GWRT scheme is incorporated into a GCM. Shortwave cloud forcing refers to the difference between the solar flux absorbed by the system under cloud cover minus that for clear sky conditions. Future research efforts should focus on extending the observations of high ice clouds into the Tropics and arctic regions. This observational data is essential to the development of a sound parameterization of high ice cloud horizontal inhomogeneity. Methods such as the GWRT scheme may then be incorporated into GCMs, improving estimates of shortwave cloud forcing.

Acknowledgments. The research contained herein has been supported by Canadian Climate Change Action Fund, by DOE Grant DE-FG03-00ER62931, and by NSF Grant OPP-0084259. The University of Utah FARS data collection was supported recently by NSF Grant ATM-9528287 and NASA Grant NAG-2-1106. The authors thank Drs. Howard Barker and Keith Thompson for helpful discussions and suggestions. The Pacific Northwest National Laboratory is operated by Battelle for the U.S. Department of Energy.

REFERENCES

Ackerman, T. P., K. N. Liou, F. P. Valero, and L. Pfister, 1988: Heating rates in tropical anvils. *J. Atmos. Sci.,* **45,** 1606–1623.

Barker, H. W., 1996a: A parameterization for computing grid-averaged solar fluxes for inhomogeneous marine boundary layer clouds. Part III: Methodology and homogeneous biases. *J. Atmos. Sci.,* **53,** 2289–2303.
——, 1996b: Estimating cloud field albedo using one-dimensional series of optical depth. *J. Atmos. Sci.,* **53,** 2826–2837.
——, and Q. Fu, 1999: Modeling domain-averaged solar fluxes for an evolving tropical cloud system. *Atmos. Oceanic Opt.,* **12,** 211–217.
——, and ——, 2000: Assessment and optimization of the gamma-weighted two-stream approximation. *J. Atmos. Sci.,* **57,** 1181–1188.
——, B. A. Wielicki, and L. Parker, 1996: A parameterization for computing grid-averaged solar fluxes for inhomogeneous marine boundary layer clouds. Part II: Validation using satellite data. *J. Atmos. Sci.,* **53,** 2304–2316.
——, G. L. Stephens, and Q. Fu, 1999: The sensitivity of domain-averaged solar fluxes to assumptions about cloud geometry. *Quart. J. Roy. Meteor. Soc.,* **125,** 2127–2152.
Briegleb, B., and V. Ramanathan, 1982: Spectral and diurnal variations in clear sky planetary albedo. *J. Appl. Meteor.,* **21,** 1160–1171.
Cahalan, R. F., W. Ridgeway, W. J. Wiscombe, T. L. Bell, and J. B. Snider, 1994a: The albedo of fractal stratocumulus clouds. *J. Atmos. Sci.,* **51,** 2434–2455.
——, ——, ——, S. Gollmer, and Harshvardhan, 1994b: Independent pixel and Monte Carlo estimates of stratocumulus albedo. *J. Atmos. Sci.,* **51,** 3776–3790.
Cairns, B., A. A. Lacis, and B. E. Carlson, 2000: Absorption within inhomogeneous clouds and its parameterization in general circulation models. *J. Atmos. Sci.,* **57,** 700–714.
Comstock, J. M., and K. Sassen, 2001: Retrieval of cirrus cloud radiative and backscattering properties using combined lidar and infrared radiometer (LIRAD) measurements. *J. Atmos. Oceanic Technol.,* **18,** 1658–1673.
Considine, G., J. A. Curry, and B. Wielicki, 1997: Modeling cloud fraction and horizontal variability in marine boundary layer clouds. *J. Geophys. Res.,* **102,** 13 517–13 525.
Evans, K. F., 1993: Two-dimensional radiative transfer in cloudy atmospheres: The spherical harmonic, spatial grid method. *J. Atmos. Sci.,* **50,** 3111–3124.
Fu, Q., 1996: An accurate parameterization of the solar radiative properties of cirrus clouds for climate models. *J. Climate,* **9,** 2058–2082.
——, and K. N. Liou, 1992: On the correlated k-distribution method for radiative transfer in nonhomogeneous atmospheres. *J. Atmos. Sci.,* **49,** 2139–2156.
——, and ——, 1993: Parameterization of the radiative properties of cirrus clouds. *J. Atmos. Sci.,* **50,** 2008–2025.
——, P. Yang, and W. B. Sun, 1998: An accurate parameterization of the infrared radiative properties of cirrus clouds for climate models. *J. Climate,* **11,** 2223–2237.
——, B. Carlin, and G. Mace, 2000a: Cirrus horizontal inhomogeneity and OLR bias. *Geophys. Res. Lett.,* **27,** 3341–3344.
——, M. Cribb, H. Barker, S. Krueger, and A. Grossman, 2000b: Cloud geometry effects on atmospheric solar absorption. *J. Atmos. Sci.,* **57,** 1156–1168.
Hahn, C. J., W. B. Rossow, and S. G. Warren, 2001: ISCCP cloud properties associated with standard cloud types identified in individual surface observations. *J. Climate,* **14,** 11–28.
Harshvardan, and D. A. Randall, 1985: Comments on ''The parameterization of radiation for numerical weather prediction and climate models.'' *Mon. Wea. Rev.,* **113,** 1832–1833.
Hartmann, D. L., M. E. Ockhart-Bell, and M. L. Michelsen, 1992: The effect of cloud type on earth's energy balance: Global analysis. *J. Climate,* **5,** 1281–1304.
Heymsfield, A. J., and J. Iaquinta, 2000: Cirrus crystal terminal velocities. *J. Atmos. Sci.,* **57,** 916–938.
Lohmann, U., and E. Roeckner, 1995: Influence of cirrus cloud radiative forcing on climate and climate sensitivity in a general circulation model. *J. Geophys. Res.,* **100,** 16 305–16 323.
Mace, G. G., T. P. Ackerman, P. Minnis, and D. F. Young, 1998: Cirrus layer microphysical properties derived from surface-based millimeter radar and infrared interferometer data. *J. Geophys. Res.,* **103,** 23 207–23 216.
Matrosov, S. Y., B. W. Orr, R. A. Kropfli, and J. B. Snider, 1994: Retrieval of vertical profiles of cirrus cloud microphysical parameters from Doppler radar and infrared radiometer measurements. *J. Appl. Meteor.,* **33,** 617–626.
Mitchell, D. L., 1996: Use of mass- and area-dimensional power laws for determining precipitation particle terminal velocities. *J. Atmos. Sci.,* **53,** 617–626.
Oreopoulos, L., and R. Davies, 1998a: Plane parallel biases from satellite observation. Part I: Dependence on resolution and other factors. *J. Climate,* **11,** 919–932.
——, and ——, 1998b: Plane parallel biases from satellite observation. Part II: Parameterization for bias removal. *J. Climate,* **11,** 933–944.
——, and H. W. Barker, 1999: Accounting for subgrid-scale cloud variability in a multi-layer 1D solar radiative transfer algorithm. *Quart. J. Roy. Meteor. Soc.,* **125,** 301–330.
Pincus, R., S. A. McFarlane, and S. A. Klein, 1999: Albedo bias and the horizontal variability of clouds in subtropical marine boundary layers: Observation from ships and satellites. *J. Geophys. Res.,* **104,** 6183–6191.
Platt, C. M. R., 1973: Lidar and radiometric observations of cirrus clouds. *J. Atmos. Sci.,* **30,** 1191–1204.
Pomroy, H. R., and A. J. Illingworth, 2000: Ice cloud inhomogeneity: Quantifying bias in emissivity from radar observations. *Geophys. Res. Lett.,* **27,** 2101–2104.
Sassen, K., 2001: Cirrus clouds: A modern perspective. *Cirrus,* D. Lynch et al., Eds., Oxford University Press, 11–40.
——, and B. S. Cho, 1992: Subvisual/thin cirrus dataset for satellite verification and climatological research. *J. Appl. Meteor.,* **31,** 1275–1285.
——, and J. M. Comstock, 2001: A midlatitude cirrus cloud climatology from the facility for atmospheric remote sensing. Part III: Radiative properties. *J. Atmos. Sci.,* **58,** 2113–2127.
——, J. M. Barnett, Z. Wang, and G. G. Mace, 2001: Cloud and aerosol research capabilities at FARS: The facility for atmospheric remote sensing. *Bull. Amer. Meteor. Soc.,* **82,** 1119–1138.
Smith, W. L., X. L. Ma, S. A. Ackerman, H. E. Revercomb, and R. O. Knuteson, 1993: Remote sensing cloud properties from high spectral resolution infrared observations. *J. Atmos. Sci.,* **50,** 1708–1720.
Stephens, G. L., 1985: Reply. *Mon. Wea. Rev.,* **113,** 1834–1835.
——, 1988: Radiative transfer through arbitrary shaped optical media. Part I: A general method of solution. *J. Atmos. Sci.,* **45,** 1818–1836.
——, S.-C. Tsay, P. W. Stackhouse, and P. J. Flateau, 1990: The relevance of the microphysical and radiative properties of cirrus clouds to climate and climate feedback. *J. Atmos. Sci.,* **47,** 1742–1753.
Tiedtke, M., 1996: An extension of cloud-radiation parameterization in the ECMWF model: The representation of subgrid-scale variations of optical depth. *Mon. Wea. Rev.,* **124,** 745–750.
Weinman, J. A., and P. N. Swarztauber, 1968: Albedo of a stratified medium of isotropically scattering particles. *J. Atmos. Sci.,* **25,** 497–501.